Article

Topological Chern vectors in three-dimensional photonic crystals

https://doi.org/10.1038/s41586-022-05077-2

Received: 4 December 2021

Accepted: 6 July 2022

Published online: 28 September 2022

Check for updates

Gui-Geng Liu[1,7], Zhen Gao[2,7], Qiang Wang[1], Xiang Xi[2], Yuan-Hang Hu[3], Maoren Wang[3], Chengqi Liu[3], Xiao Lin[4], Longjiang Deng[3], Shengyuan A. Yang[5], Peiheng Zhou[3]✉, Yihao Yang[4]✉, Yidong Chong[1,6]✉ & Baile Zhang[1,6]✉

The paradigmatic example of a topological phase of matter, the two-dimensional Chern insulator[1–5], is characterized by a topological invariant consisting of a single integer, the scalar Chern number. Extending the Chern insulator phase from two to three dimensions requires generalization of the Chern number to a three-vector[6,7], similar to the three-dimensional (3D) quantum Hall effect[8–13]. Such Chern vectors for 3D Chern insulators have never been explored experimentally. Here we use magnetically tunable 3D photonic crystals to achieve the experimental demonstration of Chern vectors and their topological surface states. We demonstrate Chern vector magnitudes of up to six, higher than all scalar Chern numbers previously realized in topological materials. The isofrequency contours formed by the topological surface states in the surface Brillouin zone form torus knots or links, whose characteristic integers are determined by the Chern vectors. We demonstrate a sample with surface states forming a (2, 2) torus link or Hopf link in the surface Brillouin zone, which is topologically distinct from the surface states of other 3D topological phases. These results establish the Chern vector as an intrinsic bulk topological invariant in 3D topological materials, with surface states possessing unique topological characteristics.

Since its introduction in 1988, the two-dimensional (2D) Haldane model[1] has served as a prototype for the Chern insulator phase, establishing the concept of band topology as an intrinsic property of materials. Unlike the quantum Hall effect[14], which is based on Landau-level quantization induced by a strong external magnetic field, the Haldane model describes how a Chern insulator can arise via time-reversal symmetry breaking in a crystal. This has guided the theoretical and experimental discoveries of many 2D topological materials, including Chern insulators[2–5] as well as the quantum spin Hall effect, a time-reversal-symmetry-invariant 2D topological insulator that originated from consideration of two overlaid Haldane models[15,16]. In parallel, the ideas behind the Haldane model have been translated from condensed-matter systems to classical wave systems, giving rise to the fields of topological photonics[17–19] and topological acoustics[20,21]. These classical wave realizations, called photonic or acoustic topological insulators, exhibit topologically non-trivial band structures and topological edge states like their condensed-matter counterparts, but lack certain features such as quantized Hall conductance[14].

The idea of intrinsic band topology has been extended to numerous three-dimensional (3D) topological materials in the past decade[6,7,15,16,22–30]. For example, 2D quantum spin Hall insulators can be stacked to form a weak 3D topological insulator[15,16] that hosts topological surface states on some surfaces, and a further generalization yields strong 3D topological insulators with topological surface states on all surfaces[15,16]. Phase transitions between topologically distinct 3D insulators are mediated by topological semi-metal phases[30] such as Weyl semi-metals, which host Fermi arc surface states[22,23]. However, Chern insulators themselves have markedly lagged behind in experimental realization. A 2D Chern insulator in a real crystalline material was implemented only in 2013, using a thin film of a 3D strong topological insulator[2]. There has been no realization of a 3D Chern insulator to date.

Previous theories have established that a 3D Chern insulator is characterized by a Chern vector consisting of a vector of three Chern numbers[6,7], $\mathbf{C} = (C_x, C_y, C_z)$, similar to the 3D quantum Hall effect[8,9] but as an intrinsic material property not associated with Landau levels. The multicomponent nature of the Chern vector leads to a generalization of the topological bulk-boundary correspondence principle from one-dimensional boundaries (edge states) to 2D boundaries (surface states); as we show below, the resulting surface states can form non-trivial torus knots or torus links on the 2D surface Brillouin zone (BZ). Moreover, a 3D Chern insulator can exhibit phase transitions to Weyl semi-metals[27–30] through a process whereby a non-trivial

[1]Division of Physics and Applied Physics, School of Physical and Mathematical Sciences, Nanyang Technological University, Singapore, Singapore. [2]Department of Electronic and Electrical Engineering, Southern University of Science and Technology, Shenzhen, China. [3]National Engineering Research Center of Electromagnetic Radiation Control Materials, Key Laboratory of Multi-spectral Absorbing Materials and Structures of Ministry of Education, University of Electronic Science and Technology of China, Chengdu, China. [4]Interdisciplinary Center for Quantum Information, State Key Laboratory of Modern Optical Instrumentation, ZJU-Hangzhou Global Science and Technology Innovation Center, College of Information Science and Electronic Engineering, ZJU-UIUC Institute, Zhejiang University, Hangzhou, China. [5]Research Laboratory for Quantum Materials, Singapore University of Technology and Design, Singapore, Singapore. [6]Centre for Disruptive Photonic Technologies, The Photonics Institute, Nanyang Technological University, Singapore, Singapore. [7]These authors contributed equally: Gui-Geng Liu, Zhen Gao. ✉e-mail: phzhou@uestc.edu.cn; yangyihao@zju.edu.cn; yidong@ntu.edu.sg; blzhang@ntu.edu.sg

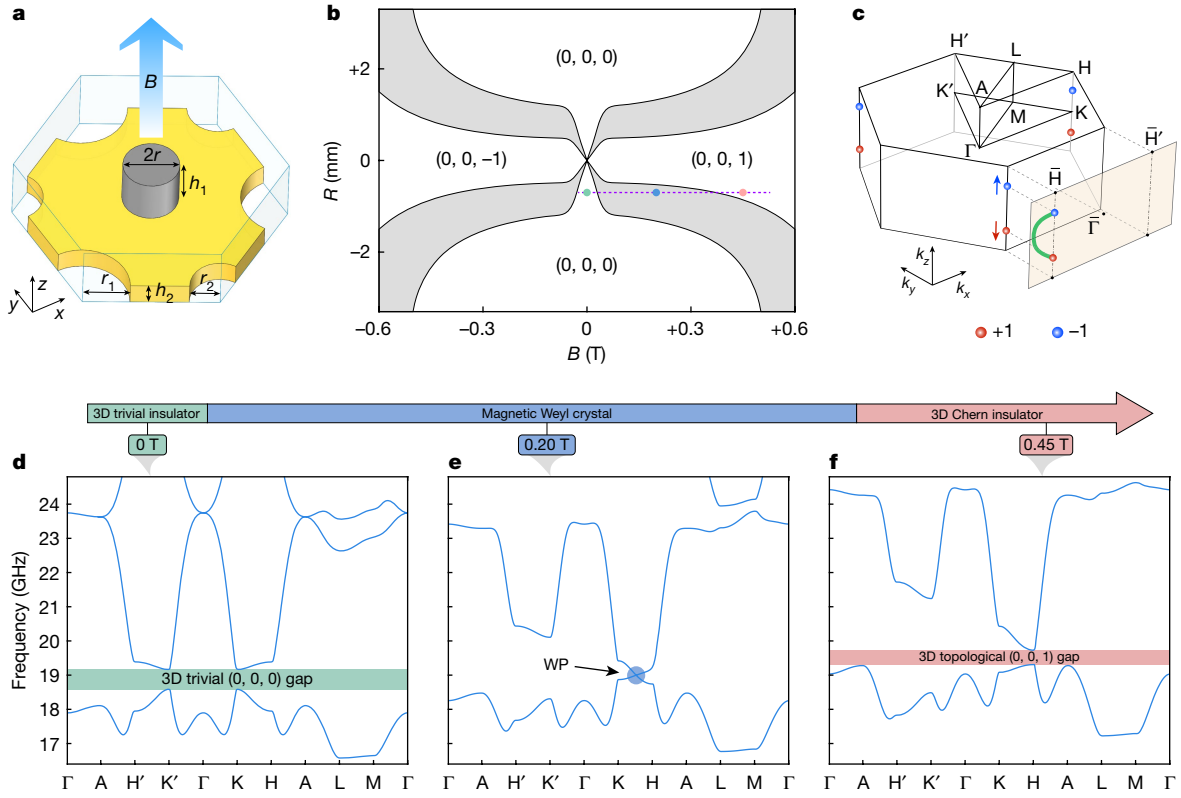

Fig. 1 | Photonic design of a 3D Chern insulator. a, Unit cell of a gyromagnetic photonic crystal biased by external magnetic field B. The lattice constant in the x–y plane is $a = 10$ mm, and periodicity along z is $h = 3$ mm. $r = 1.2$ mm, $h_1 = 2.0$ mm, $h_2 = 1.0$ mm. **b**, Phase diagram of the photonic crystal. Grey regions represent Weyl semi-metal phases hosting two WPs. **c**, Bulk BZ and (010) surface BZ. Red and blue arrows indicate WP movement directions with enhancement of B. **d**–**f**, Band diagrams of the photonic crystal with $R = -0.7$ mm ($r_1 = 2.0$ mm, $r_2 = 1.3$ mm) and $B = 0$ T (**d**), 0.20 T (**e**) or 0.45 T (**f**).

Chern vector emerges from a pair of Weyl points (WPs) with opposite charges, or vice versa. Such a topological phase transition has never been observed experimentally.

Here, we present an experimental study of magnetically tunable photonic crystals with non-trivial Chern vectors. The photonic crystal incorporates gyromagnetic materials to break the time-reversal symmetry[17–19,31]. Using a combination of bulk and surface measurements, we directly observe the topological phase transition from 3D trivial insulators to 3D Chern insulators, mediated by ideal Weyl phases that can host a single Fermi arc (the simplest possible Fermi arc configuration), which has never been seen experimentally[24–26]. By modulation of the system along a spatial axis z, we achieve a Chern vector with z-component $C_z = 6$, which is very high when compared to all scalar Chern numbers previously realized in gapped[2–5] or gapless[23–26] topological materials. We further demonstrate topological surface states between samples with perpendicular Chern vectors, which form a (2, 2) torus link (a Hopf link) in the surface BZ. Notably, this situation is topologically distinct from the limiting case of an isolated stack of decoupled 2D Chern insulators. To our knowledge, the classification of Chern insulator surface states in terms of knot theory has never previously been explored.

Unit Chern vector

We start from a photonic crystal unit cell consisting of a gyromagnetic rod and a metallic plate perforated with holes, as depicted in Fig. 1a (see Methods and Extended Data Fig. 1 for parameters of the gyromagnetic material). The holes, positioned at the two sets of inequivalent corners of the hexagonal unit cell with radii of r_1 and r_2, introduce interlayer coupling and break the in-plane inversion symmetry. Keeping $r_1 + r_2 = 3.3$ mm fixed, the difference between the hole radii, $R = r_2 - r_1$, characterizes the degree of inversion symmetry breaking. A uniform magnetic field (similar to the role of magnetic fields in ref. [3]) is applied along the z axis to magnetize the gyromagnetic rods, and field strength B characterizes the degree of time-reversal symmetry breaking.

As R and B vary, the photonic crystal shows the phase diagram seen in Fig. 1b, with trivial insulators, 3D Chern insulators and Weyl phases. At fixed $R = -0.7$ mm (that is, $r_1 = 2$ mm, $r_2 = 1.3$ mm), tuning of B allows us to access all three distinct topological phases, as indicated by the purple dashed line in Fig. 1b (see Methods and Extended Data Fig. 2 for calculation of Chern vectors, and Extended Data Fig. 3 for a qualitative tight-binding model). At zero magnetic field, the photonic crystal has a 3D trivial bandgap from 18.6 to 19.2 GHz, as shown in Fig. 1d.

Over a wide range of magnetic fields (roughly 0.03–0.355 T), the photonic crystal behaves like a gapless magnetic Weyl semi-metal. For example, at $B = 0.2$ T, the simulated band structure (Fig. 1e) has two bands linearly intersecting at momenta $(k_x, k_y, k_z) = (4\pi/3a, 0, \pm 0.53\pi/h)$ along the KH line in the bulk BZ, forming a single pair of WPs. The existence of a single pair of WPs, the minimum possible, can occur only in a time-reversal symmetry-broken system[23]. Because the WPs carry opposite topological charges (Chern numbers), their projections on the surface BZ are connected by a Fermi arc of surface states (Fig. 1c). A similar single pair of WPs was previously observed in a cold atom experiment[32], but that lattice was effectively boundary free so no Fermi arc could be probed. Simulations show that as magnetic field strength gradually increases, the system remains in the Weyl phase, the two WPs move in opposite directions (indicated by arrows in Fig. 1c) and the Fermi arc lengthens. At the critical magnetic field strength of $B = 0.355$ T, the two WPs merge at the high-symmetry point H.

The annihilation of the WPs at H corresponds to a topological transition from the Weyl phase to a non-trivial insulating phase—a 3D Chern insulator. Figure 1f shows the calculated band diagram at $B = 0.45$ T,

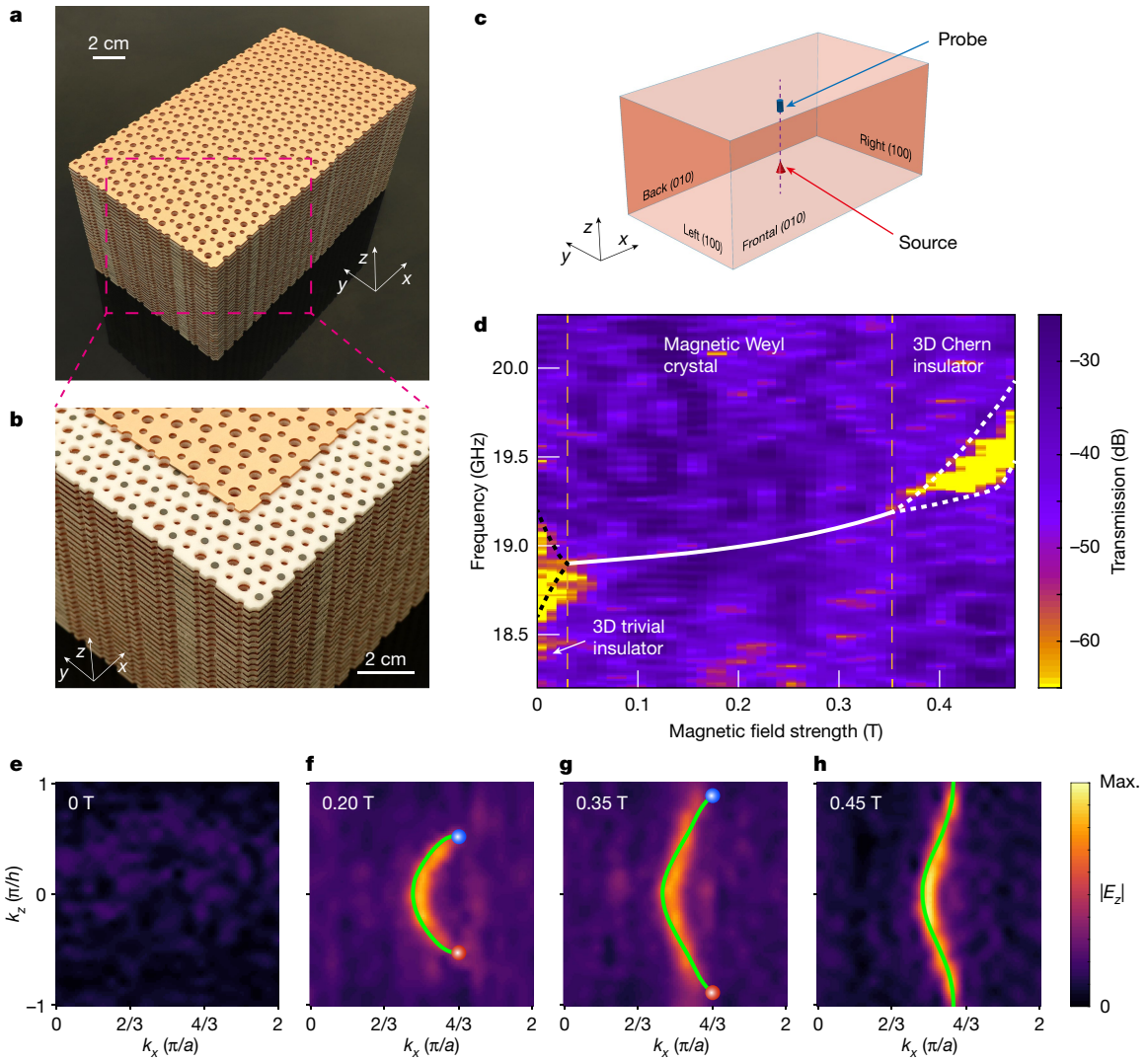

Fig. 2 | Observation of topological bandgap opening with WP pair annihilation. a, Photograph of a fabricated experimental sample. The sample has 33 layers in the z direction and 22 (14) unit cells in the x (y) direction. **b**, Close-up view of the sample; the first copper plate on the top has been moved for clarity. The gyromagnetic rods are embedded in the dielectric foam to fix their positions. **c**, Experimental set-up for measurement of bulk transmission. The source and probe are inserted from the centres of the bottom and top surfaces, at 2 cm depth. **d**, Measured bulk transmissions under different biasing magnetic fields. Solid white line indicates calculated WP frequency; the black and white dashed lines enclose the complete 3D trivial and 3D Chern bandgap, respectively. Phase transition from a 3D trivial insulator to a gapless Weyl crystal and a gapped 3D Chern insulator occurred at $B = 0.03$ T and 0.355 T, respectively. **e**–**h**, Measured surface intensity on the frontal (010) plane for biasing magnetic field strengths and frequencies of 0 T at 18.9 GHz (**e**), 0.20 T at 19.0 GHz (**f**), 0.35 T at 19.15 GHz (**g**) and 0.45 T at 19.6 GHz (**h**). Green lines indicate the simulated Fermi arc or Fermi loop surface states, and red and blue dots represent projected WPs carrying opposite topological charges.

which hosts a 3D topological bandgap from 19.3 to 19.7 GHz. The calculated Chern vector **C** = (0, 0, 1) is labelled in the phase diagram of Fig. 1b. The direction of the Chern vector is fixed along the z axis (Methods and Extended Data Fig. 4).

The experimental sample is shown in Fig. 2a,b (Methods and Extended Data Fig. 5). It is magnetically biased along the z axis by an external electromagnet. To measure bulk transmission within the sample, we insert two dipole antennae (acting as a probe and a source, respectively) into the bulk using the experimental set-up shown in Fig. 2c. The point-like source excites almost all wavevectors in bulk. By continuously tuning B from 0 to 0.475 T we obtain the bulk transmission plot shown in Fig. 2d, which exhibits closing of a complete photonic bandgap at around $B = 0.05$ T and its subsequent reopening of more than 0.36 T. These correspond to the two predicted topological phase transitions from the 3D trivial insulator phase to the gapless Weyl phase and, subsequently, to a 3D Chern insulator. For comparison, the first-principles numerical calculation shows a trivial insulator phase (with a complete 3D bandgap, bounded by two dashed black lines in Fig. 2d) of less than 0.03 T, a gapless Weyl phase from 0.030 to 0.355 T (with Weyl frequencies indicated by the solid white line in Fig. 2d) and a 3D Chern insulator phase of more than 0.355 T (with a complete 3D bandgap, bounded by two dashed white lines in Fig. 2d). The experimental and numerical results are in good agreement.

Next, we studied the topological surface states and their dependence on the biasing magnetic field. We cover the frontal (010) surface (parallel to the x–z plane) of the photonic crystal with a copper cladding, which acts as a trivial photonic bandgap material, while wrapping the other surfaces with microwave absorbers. A point source is placed near the centre of the frontal (010) surface to excite surface states. The field distributions on the surface are mapped out using a near-field scanning probe (Methods) and, subsequently, Fourier transformed to form surface dispersion contours.

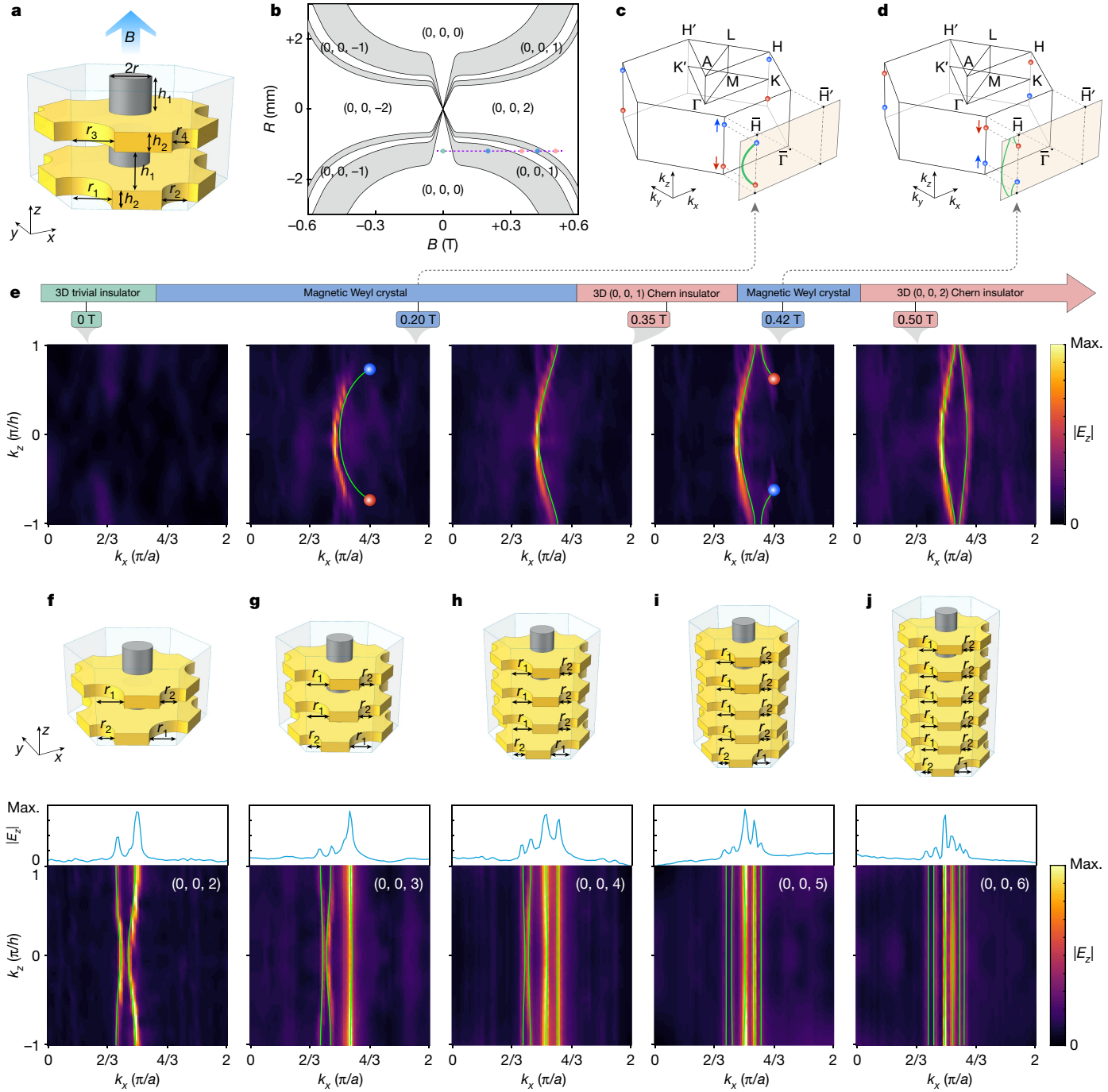

Fig. 3 | Photonic 3D Chern insulators with large Chern vectors. a, Unit cell of the photonic crystal under modulation of hole radii in two adjacent layers. $r = 1.2$ mm, $h_1 = 2$ mm, $h_2 = 1$ mm. The lattice constant in the x–y plane is $a = 10$ mm, and periodicity along z is $h = 6$ mm. Magnetic field B is applied along the $+z$ axis. **b**, Phase diagram of the photonic crystal. Grey regions represent Weyl semi-metal phases hosting two WPs. **c**,**d**, Bulk BZ and (010) surface BZ for $B = 0.20$ T (**c**) and $B = 0.42$ T (**d**). **e**, Measured surface intensity for biasing magnetic field strengths of 0 T (at 18.9 GHz), 0.20 T (at 19.1 GHz), 0.35 T (at 19.3 GHz), 0.42 T (at 19.4 GHz) and 0.50 T (at 19.8 GHz). Green lines indicate the simulated Fermi arc or Fermi loop surface states, and red and blue dots represent projected WPs carrying opposite topological charges. **f**–**j**, Top: unit cell of the photonic crystal with Chern vector (0, 0, 2) (**f**), (0, 0, 3) (**g**), (0, 0, 4) (**h**), (0, 0, 5) (**i**) and (0, 0, 6) (**j**). Hole radii are $r_1 = 2.0$ mm and $r_2 = 1.3$ mm. Bottom: measured surface intensity for biasing magnetic field 0.45 T along the $+z$ axis at frequency 19.6 GHz. Green lines represent simulated Fermi loops. Middle: measured surface intensity extracted from bottom panels at $k_z = \pi/h$, where h is the periodicity along z for each unit cell.

For $B = 0$ there is a negligible surface intensity at 18.9 GHz within the calculated bandgap (Fig. 2e), consistent with the photonic crystal being in the 3D trivial insulator phase. For $B = 0.2$ T the photonic crystal is in the Weyl phase (Fig. 2d); Fig. 2f shows the surface intensity at Weyl frequency of 19.0 GHz, which forms a single open arc connecting the projections of the two WPs, consistent with the prediction in Fig. 1e. As we further increase B, WPs move toward the boundary of the surface BZ (as shown in Fig. 2g for $B = 0.35$ T). At $B = 0.45$ T the crystal has entered the 3D Chern insulator phase and the measured surface intensity at 19.6 GHz (within the newly opened bandgap) forms a curve

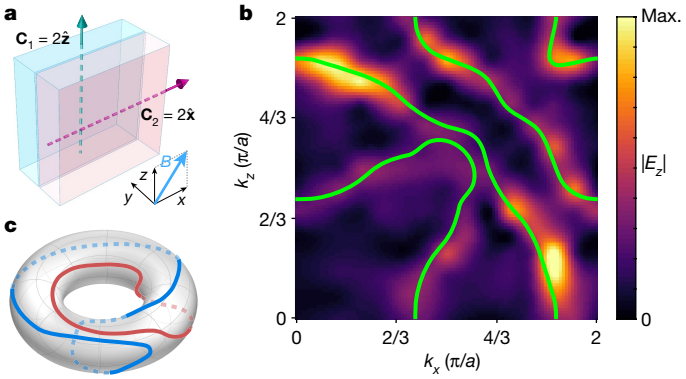

Fig. 4 | Hopf link surface states formed by perpendicular Chern vectors. **a**, Illustration of an interface between two photonic 3D Chern insulators with perpendicular Chern vectors $\mathbf{C}_1 = (0,0,2) = 2\hat{\mathbf{z}}$ and $\mathbf{C}_2 = (2,0,0) = 2\hat{\mathbf{x}}$. Magnetic field B is applied along $\hat{\mathbf{x}} + \hat{\mathbf{z}}$. **b**, Measured surface intensity at 19.6 GHz on the interface. Green lines indicate simulated Fermi loop surface states. **c**, Simulated Fermi loops wrap around the surface BZ torus to form a (2, 2)-torus link (Hopf link). Blue and red lines distinguish the two components of the torus link.

known as a surface Fermi loop[7], which winds around the surface BZ as shown in Fig. 2h. The existence and orientation of this single Fermi loop are determined by the Chern vector $\mathbf{C} = (0, 0, 1)$. Further experimental data are presented in Extended Data Fig. 6.

Large Chern vector magnitudes

Next, we increased the Chern number component C_z by application of spatial modulation along the z axis. We modulate the radii of perforated holes, as labelled by r_1, r_2, r_3, r_4 in Fig. 3a, in two adjacent layers that form a unit cell. We keep $r_1 + r_2 = 3.3$ mm and $r_3 + r_4 = 3.0$ mm fixed, and define the difference between the hole radii as $R = r_4 - r_3 = 12/7(r_2 - r_1)$. All other parameters are unchanged except the doubled periodicity along z. As R and B vary, the photonic crystal exhibits the phase diagram shown in Fig. 3b (see Methods and Extended Data Fig. 3c,d for a qualitatively similar tight-binding model). Compared with the phase diagram in Fig. 1b, there is another bandgap closing and reopening mediated by a Weyl phase, which produces a larger Chern vector $\mathbf{C} = (0, 0, \pm 2)$, implying the existence of two Fermi loops. At fixed $R = -1.2$ mm (that is, $r_1 = 2$ mm, $r_2 = 1.3$ mm, $r_3 = 2.1$ mm and $r_4 = 0.9$ mm), tuning of B allows us to access all five distinct topological phases, as indicated by the purple dashed line in Fig. 3b (see Extended Data Fig. 2d–h for Chern vector calculations and Extended Data Fig. 7a–e for band diagram simulations). We experimentally observe these phase transitions, as shown in Fig. 3e, by surface intensity measurements similar to those shown in Fig. 2e–h. Although both Weyl phases (Fig. 3c,d) host a single Fermi arc, in the latter there is an extra Fermi loop and the two WPs emerge from the boundary of the surface BZ, annihilating each other at $k_z = 0$.

We adopted another modulation scheme to construct still-larger Chern vectors. We maintained the hole radii as $r_1 = 2$ mm and $r_2 = 1.3$ mm, the same as in the sample in Fig. 2, but arranged the stacked layers in a staggered manner, as shown in the upper panels of Fig. 3f–j for unit cells constructed from two, three, four, five and six layers. This gave rise to Chern vector components $C_z = 2, 3, 4, 5$ and 6, respectively (see Extended Data Fig. 7f–j for band diagram simulations). The values of C_z were experimentally verified by counting the number of Fermi loops, as shown in the middle and lower panels of Fig. 3f–j. Our demonstrated value of $C_z = 6$ is higher than all previously realized scalar Chern numbers in both gapped[2–5] and gapless[23–26] topological materials. Further increases in C_z are possible by the addition of further modulation layers.

Torus loops and links

Chern vector $\mathbf{C} = (0, 0, m)$ induces m Fermi loops that wind around the median of the surface torus (the BZ formed by k_x and k_z) m times without crossing and, similarly, Chern vector $\mathbf{C} = (n, 0, 0)$ induces n Fermi loops winding along the longitude of the surface torus. We now consider an x–z interface between two 3D Chern insulators with perpendicular Chern vectors $m\hat{\mathbf{z}}$ and $n\hat{\mathbf{x}}$, similar to the illustration in Fig. 4a. The resulting surface states have winding numbers of m and n around the median and longitude, respectively, of the surface BZ. In knot theory[33], such an object is called an (m, n) torus knot if m and n are co-prime, or an (m, n) torus link (a link of torus knots) if m and n are not co-prime (see Methods and Extended Data Fig. 8 for a summary of torus knot theory).

We tested the above prediction by constructing an x–z interface between two photonic crystals with Chern vectors of (0, 0, 2) and (2, 0, 0)—that is, $2\hat{\mathbf{z}}$ and $2\hat{\mathbf{x}}$, as illustrated in Fig. 4a. We used the photonic crystal design in Fig. 3f for the 3D Chern insulator with Chern vector $2\hat{\mathbf{z}}$; the other 3D Chern insulator with Chern vector $2\hat{\mathbf{x}}$ is simply a duplicate rotated 90° around the y axis (see Methods and Extended Data Fig. 5e for fabricated samples). We increased the height of the gyromagnetic rods to match the periodicity along x and z, and fine-tuned the radii of the coupling holes to maximize the bandgap size (see Extended Data Fig. 9 for band diagram simulations and experimental characterization of Chern vectors). A magnetic field of $B = 0.5$ T was applied along the direction $\hat{\mathbf{x}} + \hat{\mathbf{z}}$ to magnetize both photonic crystals. As shown in Fig. 4b, the measured surface intensity shows two Fermi loops forming a (2, 2)-torus link—a so-called Hopf link—formed by two interlinked torus knots (Fig. 4c; see Extended Data Fig. 10 for a schematic of how the Hopf link forms). Other torus knots and torus links can be constructed on the basis of these principles.

Outlook

These results provide conclusive experimental evidence for 3D photonic band structures topologically characterized by the Chern vector, a vectorial generalization of the scalar Chern number. The 3D Chern insulator phase extends the 2D Chern insulator's bulk-boundary correspondence to the case of 2D boundaries, with topological surface states possessing unique characteristics. Moving forward, we can use this platform for further manipulations of the Chern vector, such as using higher spatial symmetries to realize magnetically orientable Chern vectors[31]. It would be interesting to extend the 3D Chern insulator concept from photonics[17–19] to cold atom[32,34] and condensed matter[2–5] systems, and to explore the physical implications of the linked and knotted topological surface states.

Note: when our work was under review, we noted another work reporting a Hopf link structure in the 3D BZ in a magnetic topological semi-metal[35]. Our observed Hopf link is a torus link in the 2D surface BZ, formed by topological surface states in a topological insulating phase.

Online content

Any methods, additional references, Nature Research reporting summaries, source data, extended data, supplementary information, acknowledgements, peer review information; details of author contributions and competing interests; and statements of data and code availability are available at https://doi.org/10.1038/s41586-022-05077-2.

1. Haldane, F. D. M. Model for a quantum Hall effect without Landau levels: condensed-matter realization of the "parity anomaly". *Phys. Rev. Lett.* **61**, 2015–2018 (1988).
2. Chang, C. Z. et al. Experimental observation of the quantum anomalous Hall effect in a magnetic topological insulator. *Science* **340**, 167–170 (2013).
3. Deng, Y. et al. Quantum anomalous Hall effect in intrinsic magnetic topological insulator $MnBi_2Te_4$. *Science* **367**, 895–900 (2020).

4. Zhao, Y. F. et al. Tuning the Chern number in quantum anomalous Hall insulators. *Nature* **588**, 419–423 (2020).
5. Serlin, M. et al. Intrinsic quantized anomalous Hall effect in a moiré heterostructure. *Science* **367**, 900–903 (2020).
6. Haldane, F. D. M. Berry curvature on the Fermi surface: anomalous Hall effect as a topological Fermi-liquid property. *Phys. Rev. Lett.* **93**, 206602 (2004).
7. Vanderbilt, D. *Berry Phases in Electronic Structure Theory: Electric Polarization, Orbital Magnetization and Topological Insulators* (Cambridge Univ. Press, 2018).
8. Halperin, B. I. Possible states for a three-dimensional electron gas in a strong magnetic field. *Jpn. J. Appl. Phys.* **26**, S3-3 (1987).
9. Kohmoto, M., Halperin, B. I. & Wu, Y. S. Diophantine equation for the three-dimensional quantum Hall effect. *Phys. Rev. B* **45**, 13488 (1992).
10. Balents, L. & Fisher, M. P. Chiral surface states in the bulk quantum Hall effect. *Phys. Rev. Lett.* **76**, 2782 (1996).
11. Druist, D. P., Turley, P. J., Maranowski, K. D., Gwinn, E. G. & Gossard, A. C. Observation of chiral surface states in the integer quantum Hall effect. *Phys. Rev. Lett.* **80**, 365–368 (1998).
12. Bernevig, B. A., Hughes, T. L., Raghu, S. & Arovas, D. P. Theory of the three-dimensional quantum Hall effect in graphite. *Phys. Rev. Lett.* **99**, 146804 (2007).
13. Tang, F. et al. Three-dimensional quantum Hall effect and metal–insulator transition in $ZrTe_5$. *Nature* **569**, 537–541 (2019).
14. von Klitzing, K. et al. 40 years of the quantum Hall effect. *Nat. Rev. Phys.* **2**, 397–401 (2020).
15. Hasan, M. Z. & Kane, C. L. Colloquium: topological insulators. *Rev. Mod. Phys.* **82**, 3045–3067 (2010).
16. Qi, X. L. & Zhang, S. C. Topological insulators and superconductors. *Rev. Mod. Phys.* **83**, 1057–1110 (2011).
17. Haldane, F. D. M. & Raghu, S. Possible realization of directional optical waveguides in photonic crystals with broken time-reversal symmetry. *Phys. Rev. Lett.* **100**, 013904 (2008).
18. Wang, Z., Chong, Y., Joannopoulos, J. D. & Soljačić, M. Observation of unidirectional backscattering-immune topological electromagnetic states. *Nature* **461**, 772–775 (2009).
19. Ozawa, T. et al. Topological photonics. *Rev. Mod. Phys.* **91**, 015006 (2019).
20. Yang, Z. et al. Topological acoustics. *Phys. Rev. Lett.* **114**, 114301 (2015).
21. Ma, G., Xiao, M. & Chan, C. T. Topological phases in acoustic and mechanical systems. *Nat. Rev. Phys.* **1**, 281–294 (2019).
22. Wan, X., Turner, A. M., Vishwanath, A. & Savrasov, S. Y. Topological semimetal and Fermi-arc surface states in the electronic structure of pyrochlore iridates. *Phys. Rev. B* **83**, 205101 (2011).
23. Armitage, N. P., Mele, E. J. & Vishwanath, A. Weyl and Dirac semimetals in three-dimensional solids. *Rev. Mod. Phys.* **90**, 015001 (2018).
24. Belopolski, I. et al. Discovery of topological Weyl fermion lines and drumhead surface states in a room temperature magnet. *Science* **365**, 1278–1281 (2019).
25. Liu, D. et al. Magnetic Weyl semimetal phase in a Kagomé crystal. *Science* **365**, 1282–1285 (2019).
26. Morali, N. et al. Fermi-arc diversity on surface terminations of the magnetic Weyl semimetal $Co_3Sn_2S_2$. *Science* **365**, 1286–1291 (2019).
27. Burkov, A. A. & Balents, L. Weyl semimetal in a topological insulator multilayer. *Phys. Rev. Lett.* **107**, 127205 (2011).
28. Chen, C. Z. et al. Disorder and metal-insulator transitions in Weyl semimetals. *Phys. Rev. Lett.* **115**, 246603 (2015).
29. Liu, S., Ohtsuki, T. & Shindou, R. Effect of disorder in a three-dimensional layered Chern insulator. *Phys. Rev. Lett.* **116**, 066401 (2016).
30. Xiao, J. & Yan, B. First-principles calculations for topological quantum materials. *Nat. Rev. Phys.* **3**, 283–297 (2021).
31. Devescovi, C. et al. Cubic 3D Chern photonic insulators with orientable large Chern vectors. *Nat. Commun.* **12**, 7330 (2021).
32. Wang, Z. Y. et al. Realization of an ideal Weyl semimetal band in a quantum gas with 3D spin-orbit coupling. *Science* **372**, 271–276 (2021).
33. Manturov, V. *Knot Theory* (CRC Press, 2018).
34. Jotzu, G. et al. Experimental realization of the topological Haldane model with ultracold fermions. *Nature* **515**, 237–240 (2014).
35. Belopolski, I. et al. Observation of a linked-loop quantum state in a topological magnet. *Nature* **604**, 647–652 (2022).

Methods

Numerical simulation

The bulk and surface band diagrams were numerically calculated with a finite-element method solver (COMSOL Multiphysics RF Module). The copper plates were modelled as perfect electric conductors (PECs). The surface dispersions on the front (010) surface were calculated in a supercell with 40 cells in the y direction, the two boundaries parallel to the frontal (010) surface were set as PECs and the other boundaries were set as periodic boundary conditions.

The relative permeability tensor of the gyromagnetic materials has the form $\tilde{\mu} = \begin{bmatrix} \mu_r & i\kappa & 0 \\ -i\kappa & \mu_r & 0 \\ 0 & 0 & 1 \end{bmatrix}$, where $\mu_r = 1 + \frac{(\omega_0 + i\alpha\omega)\omega_m}{(\omega_0 + i\alpha\omega)^2 - \omega^2}$, $\kappa = \frac{\omega\omega_m}{(\omega_0 + i\alpha\omega)^2 - \omega^2}$, $\omega_m = \gamma\mu_0 M_s$, $\omega_0 = \gamma\mu_0 H_0$, $\mu_0 H_0$ is the external magnetic field along the z direction, $\gamma = 1.76 \times 10^{11}\ s^{-1}T^{-1}$ is the gyromagnetic ratio, $\alpha = 0.0088$ is the damping coefficient and ω is the operating frequency. The dispersion of permeability tensor elements μ_r and κ for 0.20 and 0.45 T biasing magnetic fields is shown in Extended Data Fig. 1a,b, respectively. Because the resonance frequency of the permeability is far from the Weyl frequency or the bandgap, to facilitate simulation we ignored weak dispersion in permeability within the frequency range of interest. Take the simulation of Fig. 2d as an example: the dispersionless μ_r and κ are taken from the values of the dispersive μ_r and κ at the Weyl frequency in the gapless phase, or at the mid-gap frequency in the gapped phase. The values of μ_r and κ at different magnetic field strengths are shown in Extended Data Fig. 1c.

Calculation of Chern vector and WP charge in the photonic crystal

The topological charge (Chern number) of a WP is calculated by integrating the Berry curvatures over a surface enclosing the WP. The Berry curvature is defined as $\Omega_n(\mathbf{k}) = \nabla_{\mathbf{k}} \times A_n(\mathbf{k})$, where $A_n(\mathbf{k}) = i\langle u_{n,\mathbf{k}} | \nabla_{\mathbf{k}} | u_{n,\mathbf{k}} \rangle$ is the Berry connection and $u_{n,\mathbf{k}}$ is the Bloch state for the nth band. The topological charge of a WP is given by $\frac{1}{2\pi}\int_S \Omega_n(\mathbf{k})\mathrm{d}\mathbf{s}$, where S is a surface enclosing the WP.

A Chern number is well defined for a 2D slice of the first BZ not containing the WP. Specifically, the Chern numbers for the $\hat{\mathbf{x}}$, $\hat{\mathbf{y}}$ and $\hat{\mathbf{z}}$ momentum planes are defined as $C_{x,y,z} = \frac{1}{2\pi}\int_{S^{x,y,z}} \Omega_n^{x,y,z}\, \mathrm{d}^2k$, where $S^{x,y,z}$ are the $k_{x,y,z}$-fixed 2D BZ. In Extended Data Fig. 2a–c we show the calculated C_z for the band structure simulations in Fig. 1d–f, respectively. For example, the calculated C_z for the second band of the photonic crystal under 0.2 T magnetic field shows that $C_z(|k_z| < 0.53\pi/h) = 1$ and $C_z(|k_z| > 0.53\pi/h) = 0$. The change of C_z corresponds to the positions of WPs.

For a 3D Chern insulator, the system is globally gapped so that $C_{x,y,z}$ are well defined over the entire BZ. For example, as shown in Extended Data Fig. 2c, $C_z = 1$ is applicable to all 2D slices of BZ for the photonic crystal with 0.45 T magnetic fields. Because $C_{x,y} = 0$, the complete bandgap between the second and the third bands of the 3D photonic Chern insulator designed in Fig. 1 can be characterized by a triad of Chern numbers, or Chern vector $\mathbf{C} = (C_x, C_y, C_z) = (0, 0, 1)$.

Extended Data Fig. 2d–h shows the calculated C_z corresponding to the phase transition demonstrated in Fig. 3e.

Qualitative tight-binding models

The gyromagnetic photonic crystals proposed in the main text can be qualitatively described by tight-binding models that help to interpret the topological phases and potential phase transitions in 3D photonic crystals[36,37]. To produce the similar phases shown in Fig. 1b, a 3D Haldane model was constructed by AA-stacking 2D Haldane model layers and introducing the interlayer coupling (Extended Data Fig. 3a). For each layer, the A (purple) and B (orange) sublattice sites possessed on-site energies of $+M$ and $-M$, respectively. There is a real hopping term, t_1, between the nearest-neighbour sites (solid black lines) and a complex hopping term, $t_2\exp(i\phi)$, between the next-nearest-neighbour sites (solid purple and orange lines). The interlayer hopping terms for A and B sublattice sites are t_a (pink dashed line) and t_b (blue dashed line), respectively. The Bloch Hamiltonian of this 3D Haldane model is given by $H(\mathbf{k}) = \begin{pmatrix} \Delta^+ & \Phi^- \\ \Phi^+ & \Delta^- \end{pmatrix}$, where $\Delta^{\pm} = 2t_2\sum_{i=1,2,3}\cos(\phi \pm \mathbf{k}\cdot\mathbf{b}_i) \pm M + 2t_{a,b}\cos(k_z h)$, $\Phi^{\pm} = t_1\sum_{i=1,2,3} e^{\pm i\mathbf{k}\cdot\mathbf{a}_i}$, ($\mathbf{a}_1$, $\mathbf{a}_2$, $\mathbf{a}_3$) are the displacements from a B site to its three adjacent A sites and $\mathbf{b}_1 = \mathbf{a}_2 - \mathbf{a}_3$, $\mathbf{b}_2 = \mathbf{a}_3 - \mathbf{a}_1$, $\mathbf{b}_3 = \mathbf{a}_1 - \mathbf{a}_2$. By tuning the hopping terms, this 3D model exhibits a phase diagram shown in Extended Data Fig. 3b; M and ϕ characterize the inversion and time-reversal symmetry-breaking strengths, respectively. The phases in the diagram in Fig. 1b, including 3D Chern insulating, 3D trivial insulating and gapless Weyl phases, also emerge in this 3D Haldane model. Note that one phase present in the 3D Haldane model, but not in our photonic crystal analogue, is a Weyl phase with four WPs, but this is not important to the present study.

To demonstrate the phases shown in Fig. 3b we can also develop a 3D Haldane model with two layers in a unit cell, as shown in Extended Data Fig. 3c. By assigning different interlayer couplings for the two layers, we can obtain a more complicated phase diagram shown in Extended Data Fig. 3d. Apart from the previous phases, there are two new phases emerging: another gapless Weyl phase and another 3D Chern insulating phase with $C_z = \pm 2$.

Direction of Chern vector in the presence of tilted magnetic fields

In our designed photonic crystals, the direction of Chern vectors is determined by the stacking direction. For example, the Chern vectors in Figs. 1–3 are always in the form of $(0, 0, m)$—that is, in the z direction. Even when the external magnetic field is tilted, the direction of Chern vectors will not change. This is because, in each layer of the crystal, the upper and lower metallic plates form a parallel-plate waveguide of deep subwavelength thickness. Therefore, only the fundamental mode is guided in the parallel-plate waveguide, where E field is in the z direction and H field is in the x–y plane. The H field in the x–y plane mainly interacts with the magnetization of gyromagnetic rods along the z axis, which induces Chern vectors in the z direction. As an example, we numerically simulate in Extended Data Fig. 4 the phase diagram of the photonic crystal designed in Fig. 1, when the magnetic field $B = 0.45$ T is applied at a tilted angle. We define the angle between the x axis and the magnetic field as α. By varying the parameters R and α, the photonic crystal exhibits various phases (see phase diagram in Extended Data Fig. 4b). With $R = -0.7$ mm, the photonic crystal hosts a 3D trivial gap at $\alpha = 0$ (Extended Data Fig. 4d), a pair of WPs at $\alpha = \pi/6$ (Extended Data Fig. 4e) and a 3D Chern insulating gap at $\alpha = \pi/2$ (Extended Data Fig. 4f). Tilting will reduce the effective magnetic field in the z direction but the induced Chern vector, if non-trivial, is always in the z direction. Tilting of the magnetic field will shift WPs off the high-symmetry KH line only slightly, as shown in Extended Data Fig. 4c.

Experimental set-ups

The gyromagnetic material is yttrium iron garnet (YIG) ferrite, with relative permittivity 14.3 and dielectric loss tangent 0.0002. The measured saturation magnetization is $M_s = 1{,}780$ Gauss and the gyromagnetic resonance loss width is 35 Oe. The copper plates were prepared by coating copper of thickness 0.035 mm onto Teflon woven-glass fabric laminate. The dielectric foam (ROHACELL 31 HF) used to fix the positions of YIG rods has relative permittivity 1.04 and loss tangent 0.0025. The air holes penetrate through the copper plate layers and the dielectric foam layers, as shown in Extended Data Fig. 5a. In the measurements, uniform external magnetic fields generated by an electromagnet were applied along the z axis producing a strong gyromagnetic response in the ferrite rods, as shown in Extended Data Fig. 5c. The spatial non-uniformity of

the magnetic fields is less than 2% in the sample region, measured and calibrated using a gaussmeter (HFBTE, no. TD8620).

During measurements, two microwave dipole antennae were connected to a vector network analyser (Agilent Technologies, no. E8363C) to function as the source and probe, respectively. Complex field distributions were measured by insertion of the probe into the air holes one by one and scanning along the z direction in small steps.

The chiral propagation of surface states is demonstrated in Extended Data Fig. 6e,f. In particular, we inserted several copper pillars into the coupling holes to function as the metallic obstacles (Extended Data Fig. 5b). In Fig. 3, for large Chern vectors, to enhance the resolution and distinguish multiple Fermi loops we adopted triangular samples as shown in Extended Data Fig. 5d, where all three wall surfaces were identical. Because surface states propagate around corners robustly, the three surfaces can be treated as a single surface with more data points in Fourier transform processing. The experimental sample in Fig. 4 is shown in Extended Data Fig. 5e. A dielectric foam (ROHACELL 31 HF) of thickness 3 mm was inserted between the two photonic crystals to tune the coupling of the surface states.

Torus knot theory

In knot theory, a torus knot is a knot that can be placed on the surface of a torus without crossing itself. A torus knot is classified by two co-prime integers, m and n, which correspond to the number of times a knot wraps around the longitude and meridian of a torus, as labelled by (m, n). If m and n are not co-prime, (m, n) describes a torus link formed by a number of torus knots equal to the greatest common divisor between m and n[33]. In Extended Data Fig. 8 we plot the torus knots/links for different combinations of m and n. The simplest torus link, which consists of two non-crossing components, is the (2, 2)-torus link, or Hopf link.

Construction of perpendicular Chern vectors

The two perpendicular Chern vectors, $2\hat{\mathbf{z}}$ and $2\hat{\mathbf{x}}$, were constructed in two photonic crystals, as shown in Extended Data Fig. 9a,e, where the magnetic field was applied along the direction of $\hat{\mathbf{x}} + \hat{\mathbf{z}}$. These two photonic crystals have identical properties except for different orientations (see Extended Data Fig. 9b,f for band diagrams). When interfaced with a PEC, each photonic crystal shows two Fermi loops, as simulated and measured in Extended Data Fig. 9c,g. These Fermi loops wrap around the BZ torus surface, as shown in Extended Data Fig. 9d,h.

When two photonic crystals interface with each other, as illustrated in Fig. 4a, there are some interactions among their Fermi loops. Owing to the anti-crossing principle, the four Fermi loops will rearrange in the BZ and merge into two Fermi loops that then wrap around the torus surface as a Hopf link, as shown in Extended Data Fig. 10.

Data availability

The data in this study are available from the Digital Repository of NTU at https://doi.org/10.21979/N9/QTBDH7.

36. Slobozhanyuk, A. et al. Three-dimensional all-dielectric photonic topological insulator. *Nat. Photon.* **11**, 130–136 (2017).
37. Yang, Y. et al. Realization of a three-dimensional photonic topological insulator. *Nature* **565**, 622–626 (2019).

Acknowledgements We acknowledge funding from the Singapore National Research Foundation Competitive Research Program (grant no. NRF-CRP23-2019-0007) and Singapore Ministry of Education Academic Research Fund Tier 3 (grant no. MOE2016-T3-1-006). P.Z., Z.G. and Y.Y. acknowledge funding from the National Natural Science Foundation of China (grant nos. 52022018, 52021001, 12104211, 6101020101 and 62175215) and Chinese Academy of Engineering (grant no. 2022-XY-127).

Author contributions Y.Y. and G.-G.L. initiated the project. Q.W. performed the tight-binding calculation. G.-G.L. and X.X. performed the simulation. G.-G.L., Z.G., Y.Y. and B.Z. designed experiments. Z.G. and P.Z. fabricated samples. P.Z., Y.-H.H., M.W. and C.L. carried out measurements. G.-G.L., Y.Y., P.Z., Z.G., Q.W., X.L., X.X., L.D., S.A.Y., Y.C. and B.Z. analysed the results and wrote the manuscript. B.Z., Y.C., Y.Y. and P.Z. supervised the project.

Competing interests The authors declare no competing interests.

Additional information

Supplementary information The online version contains supplementary material available at https://doi.org/10.1038/s41586-022-05077-2.

Correspondence and requests for materials should be addressed to Peiheng Zhou, Yihao Yang, Yidong Chong or Baile Zhang.

Peer review information *Nature* thanks Alexander Khanikaev and the other, anonymous, reviewer(s) for their contribution to the peer review of this work. Peer reviewer reports are available.

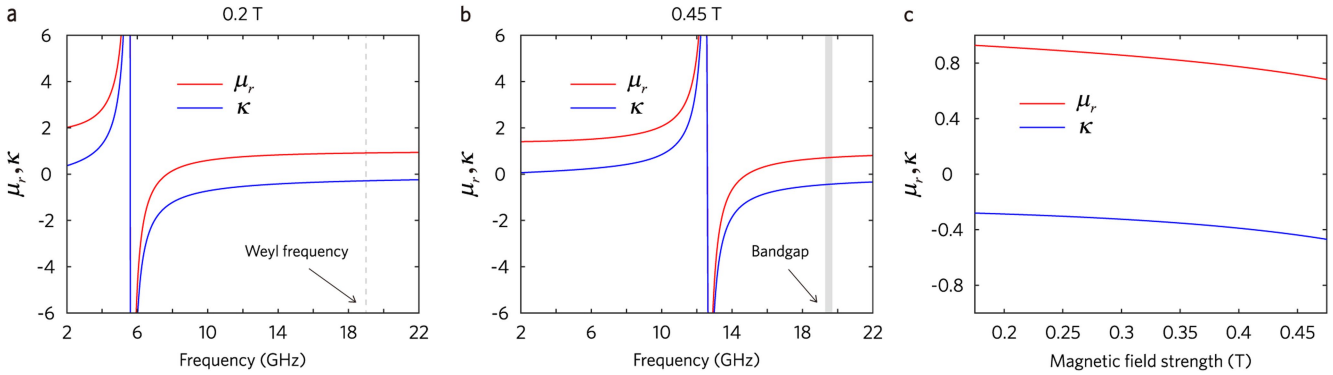

Extended Data Fig. 1 | Permeability tensor of the gyromagnetic material. **a**,**b**, Frequency-dependent elements μ_r and κ of the permeability tensor of the gyromagnetic material for $B = 0.20$ T and 0.45 T, respectively. The grey dashed line in **a** indicates the Weyl frequency in Fig. 2, and the grey rectangle in **b** indicates the bandgap of the photonic crystal in Fig. 2. **c**, Dispersionless μ_r and κ adopted in all simulations as a function of biasing magnetic fields.

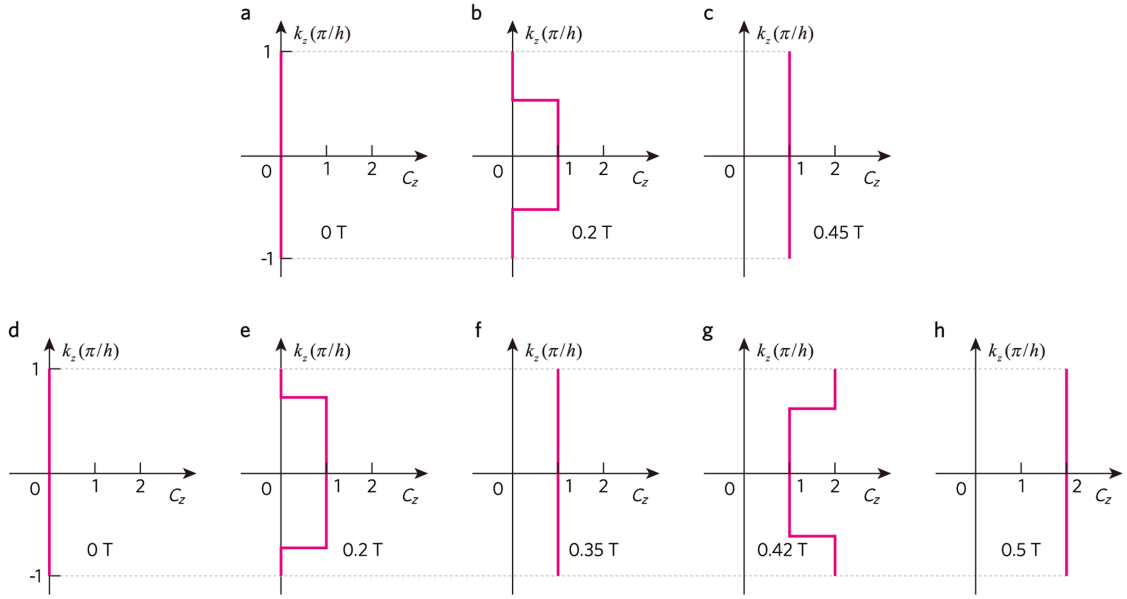

Extended Data Fig. 2 | Chern-number component C_z of photonic crystals. **a**–**c**, Chern-number component C_z calculated in the 2D BZ plane at a fixed k_z along the purple dashed line in Fig. 1b. The magnetic field B = 0 T, 0.20 T, and 0.45 T, corresponds to the band diagrams in Fig. 1d, e, and f, respectively. **d**–**h**, Chern-number component C_z calculated in the 2D BZ plane at a fixed k_z along the purple dashed line in Fig. 3b. The magnetic field B = 0 T, 0.20 T, 0.35 T, 0.42 T, and 0.50 T, corresponds to the simulated and measured surface intensities in Fig. 3e.

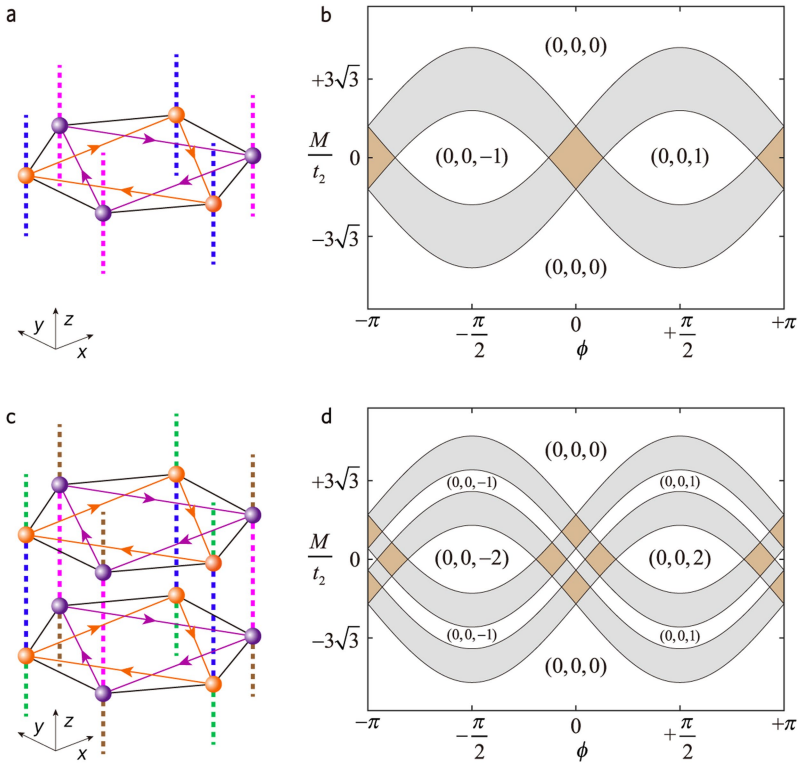

Extended Data Fig. 3 | Qualitative tight-binding models. a, Qualitative tight-binding model for the photonic crystal designed in Fig. 1. **b**, Phase diagram of the model in **a**. It exhibits a trivial 3D insulating phase and a 3D Chern insulator phase, characterized by Chern vectors of (0, 0, 0) and (0, 0, ±1), respectively. **c**, Qualitative tight-binding model with two layers in a unit cell. **d**, Phase diagram of the model in **c**. Each gapped phase has been labelled by a Chern vector. The brown and the grey regions represent the gapless Weyl semimetal phases hosting four and two WPs in the first BZ, respectively. Here, $t_2 = 1.2$, and the interlayer couplings represented by pink, blue, brown, and green dashed lines are 3, 0.5, 2, and 1.5, respectively.

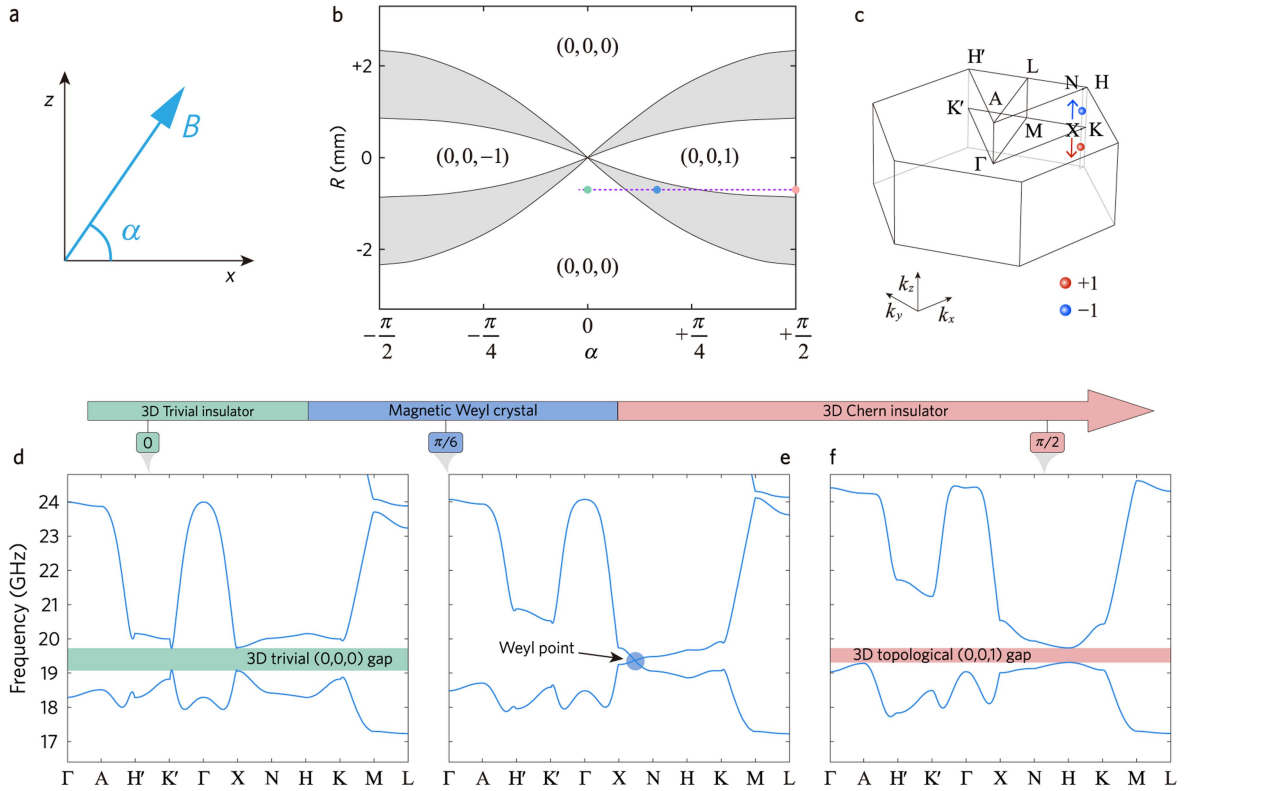

Extended Data Fig. 4 | Phase transition by rotation of magnetic fields. The photonic crystal designed in Fig. 1 is considered in the simulation as a typical example. **a**, Magnetic field rotatable in the *x*-*z* plane. **b**, Phase diagram of the photonic crystal by tuning the radius difference between two coupling holes $R = r_2 - r_1$ and the angle between the *x*-axis and the magnetic field α ($B = 0.45$ T). Grey regions: Weyl semimetal phases hosting two WPs. **c**, Bulk BZ. The blue and red dots are the two ideal WPs with opposite topological charges, when $\alpha = \pi/6$. The red and blue arrows indicate the moving directions of the WPs with the enhancement of the α. **d**–**f**, Band diagrams of the photonic crystal with $R = -0.7$ mm and α of 0, π/6, and π/2, respectively. The green rectangle in **d** represents a complete 3D trivial bandgap from 19.1 to 19.7 GHz. The blue dot in **e** denotes a WP. The red rectangle in **f** represents a complete 3D topological bandgap from 19.3 to 19.7 GHz.

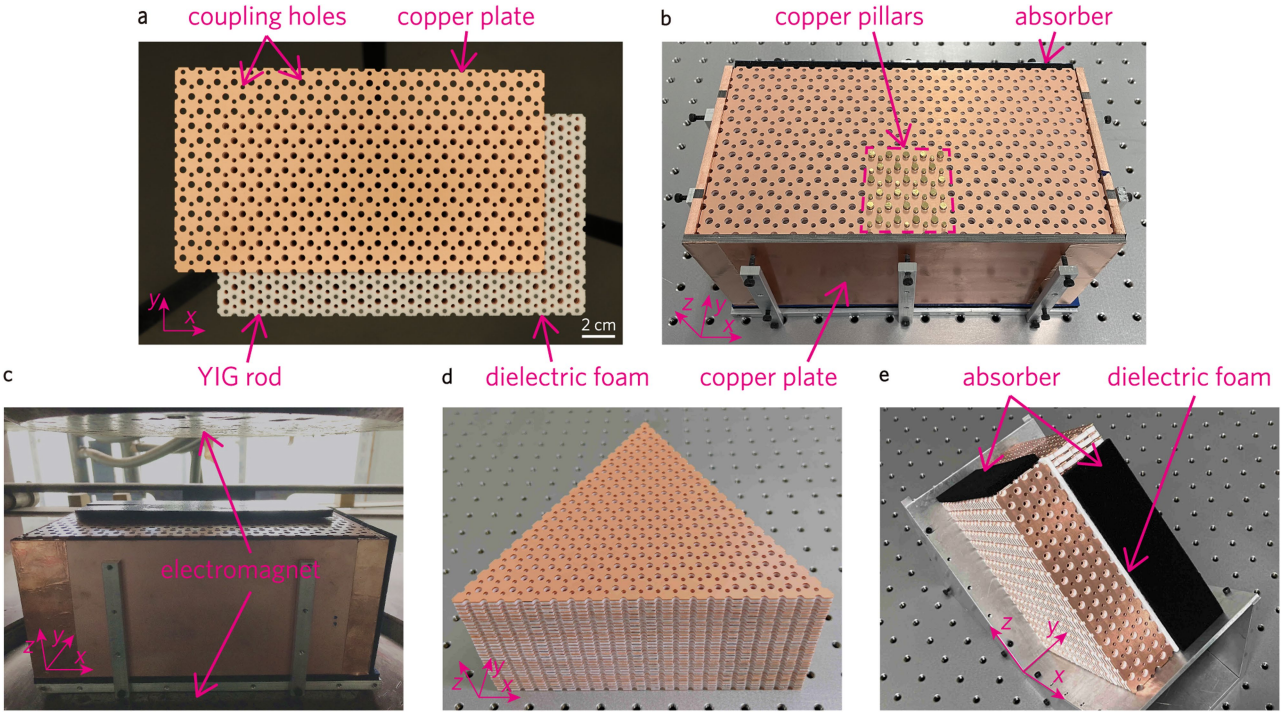

Extended Data Fig. 5 | Experimental setups. a, Top view of the fabricated sample in Fig. 2a, where the first copper plate on the top is shifted for visualization. **b**, Copper pillars inserted into the coupling holes to function as metallic obstacles. **c**, Electromagnet used to produce magnetic fields. **d**, Triangular samples whose three wall surfaces are identical. **e**, Setup of two interfaced photonic crystals with perpendicular Chern vectors used in the demonstration in Fig. 4.

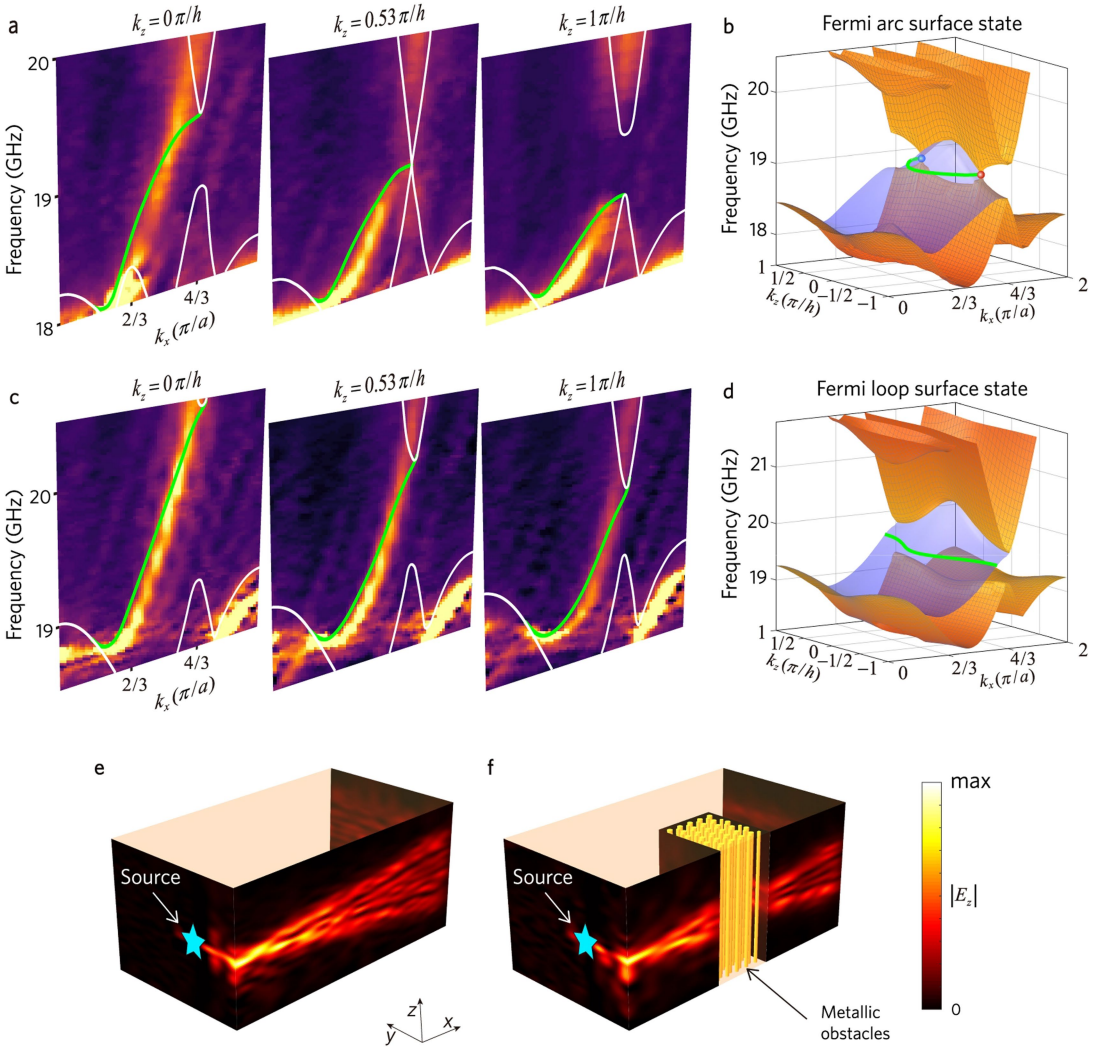

Extended Data Fig. 6 | Frequency-dependent surface dispersion and robustness of chiral surface states. a, **c**, Measured surface dispersions on the frontal (010) surface of the fabricated sample in Fig. 2 for $B = 0.20$ T and 0.45 T, respectively. Three values of $k_z = 0, 0.53\pi/h$, and $1\pi/h$ are selected. **b**, **d**, Simulated band structure on the frontal (010) surface for $B = 0.20$ T and 0.45 T, respectively. The white and green curves in **a** and **c** indicate the simulated envelopes of the projected bulk dispersions and surface dispersions, respectively. The blue curved surfaces in **b** and **d** represent the topological surface states, while the orange sheets indicate the envelopes of the projected bulk dispersions. **e**, Measured field distribution of chiral surface states in the fabricated sample in Fig. 2. The surface states are excited by a point source (cyan star) oscillating at 19.6 GHz. **f**, Measured field distribution in the same setup as in **e**, while copper pillars (yellow rods) are inserted into the sample as metallic obstacles. The frontal (010), left (100), and right (100) surfaces of the sample are covered with copper claddings, and all other surfaces with microwave absorbers. The samples are biased at 0.45 T along +z axis. The chiral surface states can propagate smoothly around the sharp corners and obstacles without scattering. The surface waves are mainly confined at their individual layers when passing around the copper pillars due to the weak dispersion along the z-axis.

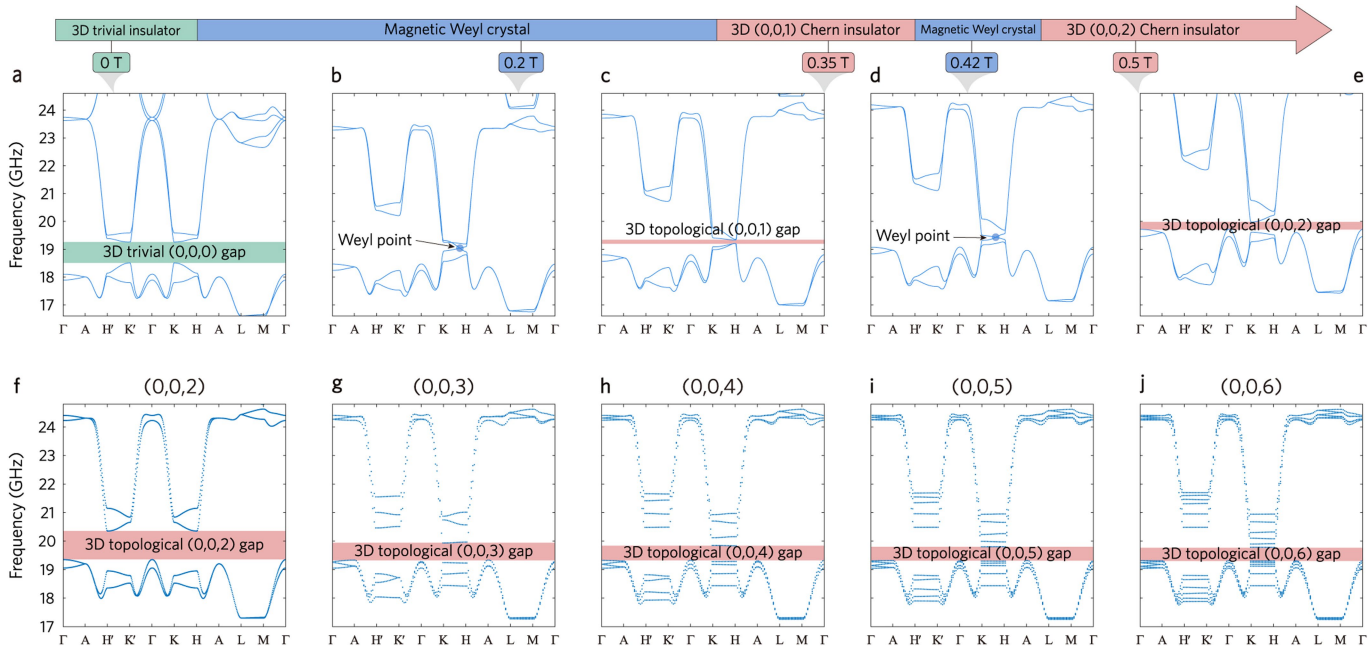

Extended Data Fig. 7 | Band diagram simulations of models in Fig. 3. a–e, Band diagrams for the photonic crystal in Fig. 3e at different magnetic fields. **f–j**, Band diagrams for different photonic crystals in Fig. 3f–j under the same magnetic field $B = 0.45$ T.

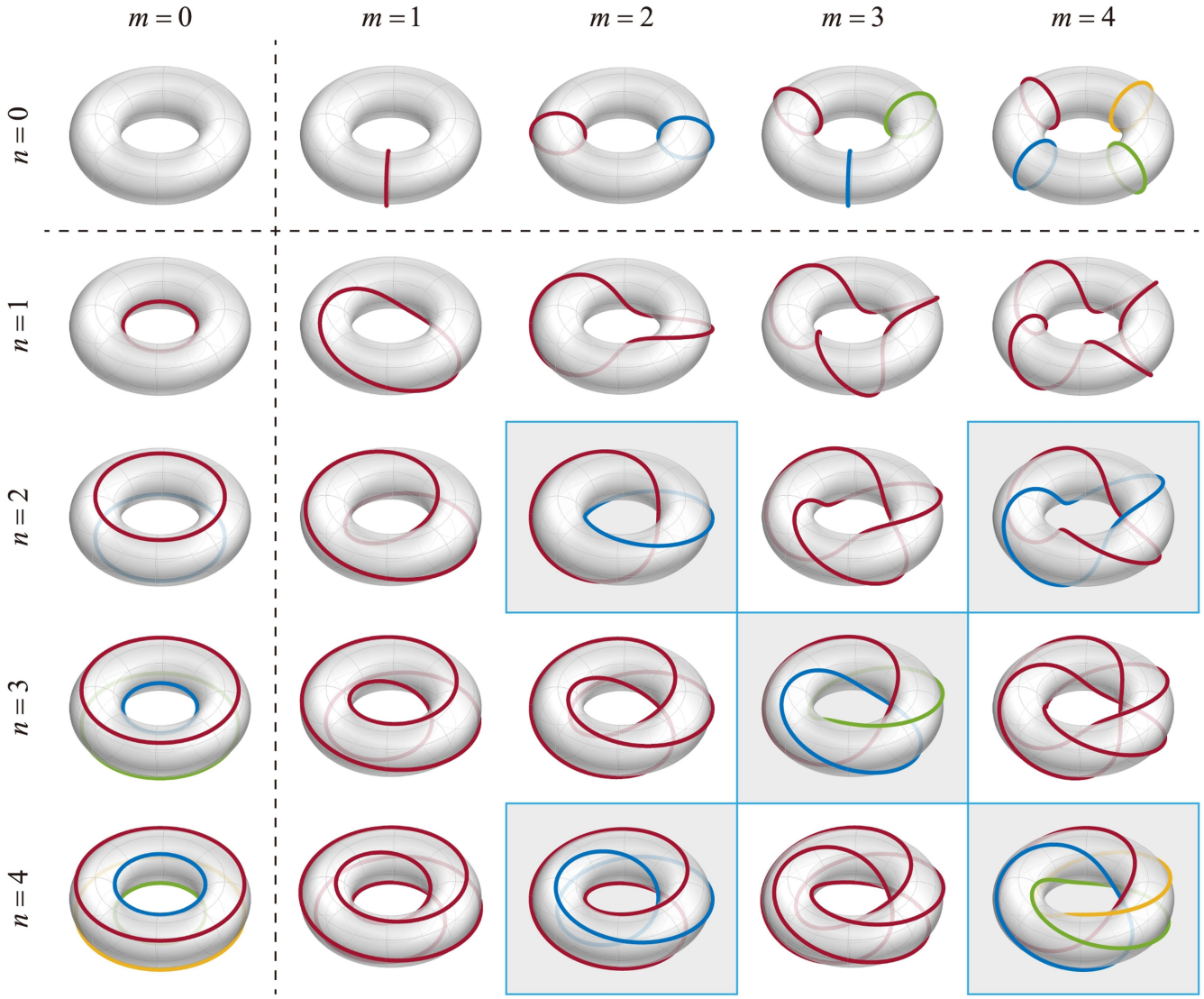

Extended Data Fig. 8 | Summary of (*m*, *n*)-torus knots/links with different combinations of *m* and *n*. The colors of red, blue, green and yellow represent the first, second, third and fourth loops that wrap around the torus surface without crossing. The links with non-coprime *m* and *n* are highlighted with grey background. The simplest link is the (2, 2)-torus link, or the Hopf link on the torus surface.

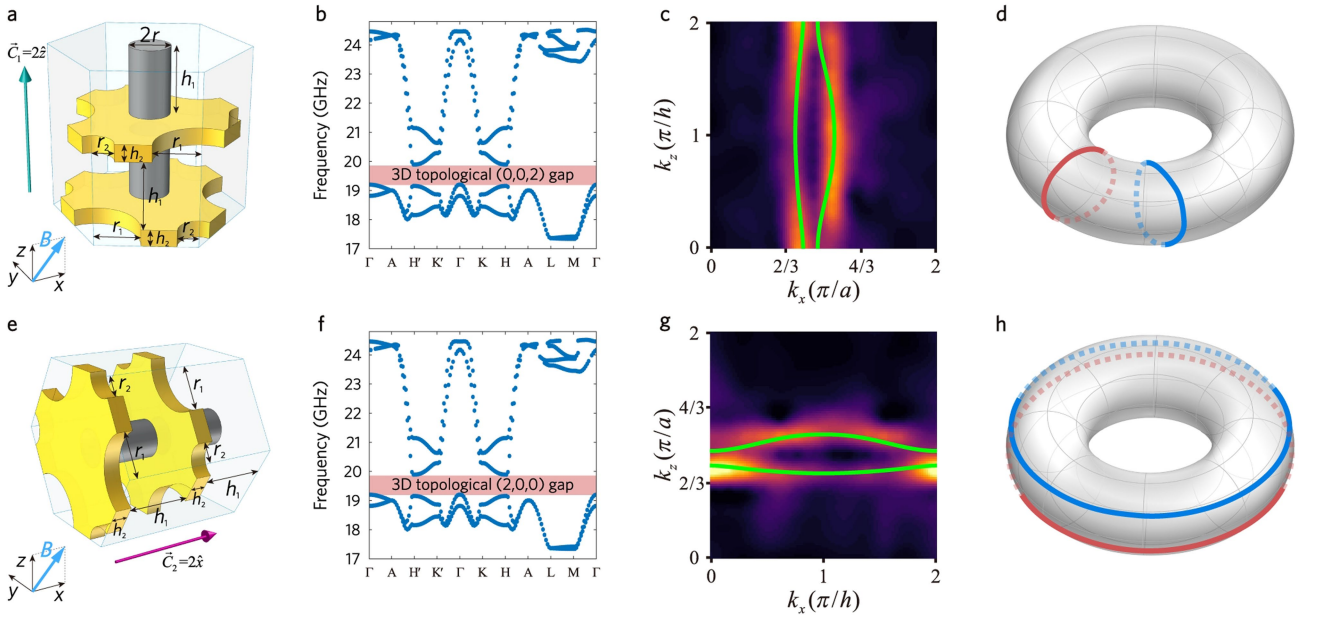

Extended Data Fig. 9 | Construction of perpendicular Chern vectors. **a**, **e**, Unit cells of the photonic crystals with Chern vectors $\mathbf{C}_1 = 2\hat{z}$ and $\mathbf{C}_2 = 2\hat{x}$, respectively. The two unit cells are identical except for different orientations. The dimensions are $r = 1.2$ mm, $h_1 = 4$ mm, $h_2 = 1$ mm, $r_1 = 2.6$ mm, and $r_2 = 1.2$ mm. The biasing magnetic field $B = 0.5$ T is oriented along the direction of $\hat{x} + \hat{z}$. **b**, **f**, Simulated band diagrams for **a**, **e**, respectively, which are identical. The bandgap is highlighted in pink. **c**, **g**, Measured surface intensity at 19.6 GHz for frontal and back (010) surfaces, respectively. The green lines indicate the simulated Fermi loop surface states. **d**, **h**, Simulated Fermi loop surface states wrap around the surface BZ in a torus geometry.

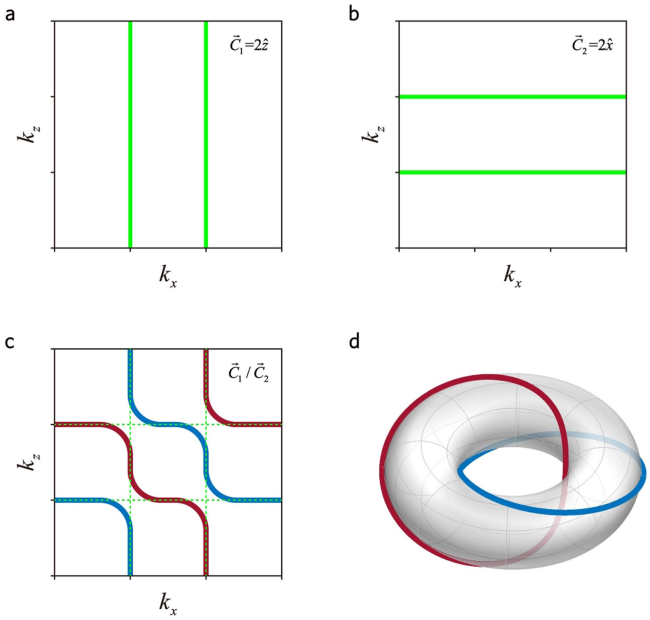

Extended Data Fig. 10 | Formation of Hopf link surface states. **a**, **b**, Illustrations for surface Fermi loops induced by Chern vectors $\mathbf{C}_1 = 2\hat{z}$ and $\mathbf{C}_2 = 2\hat{x}$, respectively. **c**, Surface Fermi loops rearranged in the presence of coupling between two photonic crystals with $\mathbf{C}_1 = 2\hat{z}$ and $\mathbf{C}_2 = 2\hat{x}$. Blue and red solid lines depict the resulted two Fermi loops around the BZ. **d**, Blue and red lines individually form a loop in a torus geometry, and the two loops form a Hopf link.